

# Energy injection in an epithelial cell monolayer via negative viscosity

Molly McCord<sup>1,2</sup>, Jacob Notbohm<sup>1,2</sup>

<sup>1</sup>Department of Mechanical Engineering, University of Wisconsin–Madison, Madison, WI, USA

<sup>2</sup>Biophysics Program, University of Wisconsin–Madison, Madison, WI, USA

## ABSTRACT

Active fluids are driven out of thermodynamic equilibrium by internally generated forces, causing complex patterns of motion. Even when both the forces and motion are measurable, it is not yet possible to relate the two, because the sources of energy injection and dissipation are often unclear. Here, we study how energy is transferred by developing a method to measure viscosity from the shear stresses and strain rates within an epithelial cell monolayer. Surprisingly, there emerged multicellular regions in which the relationship between shear stress and shear strain rate was negatively proportional, indicating a negative viscosity. We provide direct experimental evidence that the negative viscosity results from cells aligning their stresses with the orientation of the flow. Regions of negative viscosity consistently exhibited greater cell speed and vorticity, and the cells had elevated metabolic activity, indicating that negative viscosity is a mechanism for injection of surplus energy. More broadly, our study shows that negative viscosity is a useful means of quantifying the flow of energy in active materials.

## I. INTRODUCTION

A central question in active matter is how the energy injected into the system is converted to forces, and, in turn, how those forces produce motion. In an epithelial cell layer, for example, the collective flows are unpredictable, with rearrangements between neighboring cells and rotating eddies reminiscent of turbulence.<sup>1–3</sup> Although the forces producing the flow can be measured experimentally, relationships between forces and flows remain complicated. Both cell-substrate tractions and cell-cell stresses fluctuate over space.<sup>4,5</sup> In general, the direction of traction and the orientation of first principal stress do not align with the direction of cell motion.<sup>4,6</sup> As a result, some components of the tractions and stress inject energy to propel the flow, while other components act as a dissipative friction. As the physical sources for energy injection and dissipation remain unclear, it is currently impossible to predict the cell motion from the forces.

Given that inertial forces are negligible in this system, it is commonly assumed that force and motion are related through a viscosity that couples shearing stresses to flows and dissipates the active forces produced by the cells.<sup>7,8</sup> No experiment has yet measured viscosity directly in this system. Order of magnitude estimates have suggested viscosity in cell collectives to be in a wide range, from  $\sim 100$  Pa·hr to  $\sim 10,000$  Pa·hr.<sup>9,10</sup> Numerical values for viscosity in this same range have also been inferred by fitting models to experimental data.<sup>11–13</sup> Prior efforts to measure viscosity directly by plotting shearing stresses against strain rates have failed, showing no clear trends,<sup>14</sup> leaving it unclear as to whether viscosity is a physically meaningful way to describe how the active forces produced by the cells are dissipated during the collective motion.

Here, we experimentally measured the effective viscosity within an epithelial cell layer by quantifying the ratio of shear stress to strain rate. In contrast to prior work,<sup>14</sup> we quantified the viscosity at all points in space, which revealed a broad distribution of effective viscosity, with many values even becoming negative. The discovery of negative viscosity implies injection—rather than dissipation—of energy into the flow. By inspecting the relationship between stresses and strain rates, we revealed the physical mechanism for

negative viscosity and discovered that this mechanism depends on the magnitude of viscosity. We perturbed cell force production, finding that even when the flow rates were substantially altered, a substantial fraction of cells continued to exhibit negative viscosity. Finally, we revealed that cells with negative viscosity had elevated metabolism, suggesting that negative viscosity is a mechanism for injecting surplus energy into the flow.

## II. RESULTS

### A. Negative Viscosity in an Epithelial Cell Monolayer

To quantify viscosity, we began by measuring shear stress and shear strain rate in a Madin-Darby canine kidney (MDCK) cell monolayer, reasoning that their ratio would be the viscosity. To this end, we confined MDCK cells to 1 mm circular islands at a relatively low density of  $\approx 2500$  cells/mm<sup>2</sup> (Fig. 1a), which is low enough that the cells exhibit primarily fluid-like behavior.<sup>15</sup> Stresses within the cell monolayer were computed using monolayer stress microscopy,<sup>5,16,17</sup> and cell velocities were quantified using image correlation, after which the principal stresses,  $\sigma_1$  and  $\sigma_2$ , and principal strain rates,  $\dot{\epsilon}_1$  and  $\dot{\epsilon}_2$ , were computed. The shear stress and shear strain rate were then computed according to  $(\sigma_1 - \sigma_2)/2$  and  $(\dot{\epsilon}_1 - \dot{\epsilon}_2)/2$ . Representative color maps of shear stress and strain rate showed no obvious relationship between the two (Fig. 1b,c). Similarly, a scatter plot of all data points in the cell monolayer showed no correlation between the two (Appendix C, Fig. 5), consistent with prior observations.<sup>14</sup> To investigate more deeply, we considered that there may be variability over space. Spatial autocorrelations of shear stress and strain rate decayed on average over distances of 24.5  $\mu\text{m}$  (2–3 cell widths) and 31.8  $\mu\text{m}$  (3–4 cell widths), respectively (Fig. 1d). Given these relatively small spatial correlation lengths, we reasoned that it would be informative to analyze the system at spatial scales in the range of 2–4 cells. To this end, we collected the data within a  $62 \times 62 \mu\text{m}^2$  window and plotted shear stress against shear strain rate. The data showed a clear linear correlation, with the slope indicating the effective viscosity (Fig. 1e). Interestingly, in a different randomly chosen window, the linear correlation was negative, indicating the existence of a negative effective viscosity (Fig. 1f). The observation of negative viscosity indicates that the active shear stresses produced by the cells are larger than the passive viscous stresses, meaning that the active shear stresses inject energy into the flowing cell layer. This finding is reminiscent of theory and experiments in other systems, for which activity can reduce the effective viscosity.<sup>18–24</sup>

To build on our initial observations, we moved the window to all locations in the cell island, calculating the ratio of shear stress to strain rate at all locations in space. This approach revealed distinct regions with positive (blue) and negative (yellow) viscosity (Fig. 1a). To quantify the characteristic size of a region with negative viscosity, we computed the square root of the average area of a connected region having negative viscosity, which resulted in a value of 149  $\mu\text{m}$  (9–10 cells) (Fig. 1g). We also verified that the choice of window size did not substantially affect the results. To this end, we repeated the analysis, quantifying the characteristic size of a region with negative viscosity for a smaller and larger window. Results showed that the characteristic size was relatively insensitive to window size (Appendix C, Fig. 6), indicating that the results are not substantially affected by the chosen window size.

We also checked for the existence of a bulk viscosity by using the average principal stress and strain rate,  $(\sigma_1 + \sigma_2)/2$  and  $(\dot{\epsilon}_1 + \dot{\epsilon}_2)/2$ , which showed similar patterns of negative and positive values (Appendix C, Fig. 7). Given that motion within these confined islands requires cells to undergo shearing (shape changing) deformations to slide past one another, we focused on the shear viscosity for the remainder of our study. Next, to demonstrate that negative shear viscosity is a general phenomenon that exists in monolayers of other cell types, we repeated these experiments with the human keratinocyte cell line HaCaT, which exhibited negative viscosity as well (Appendix C, Fig. 8).

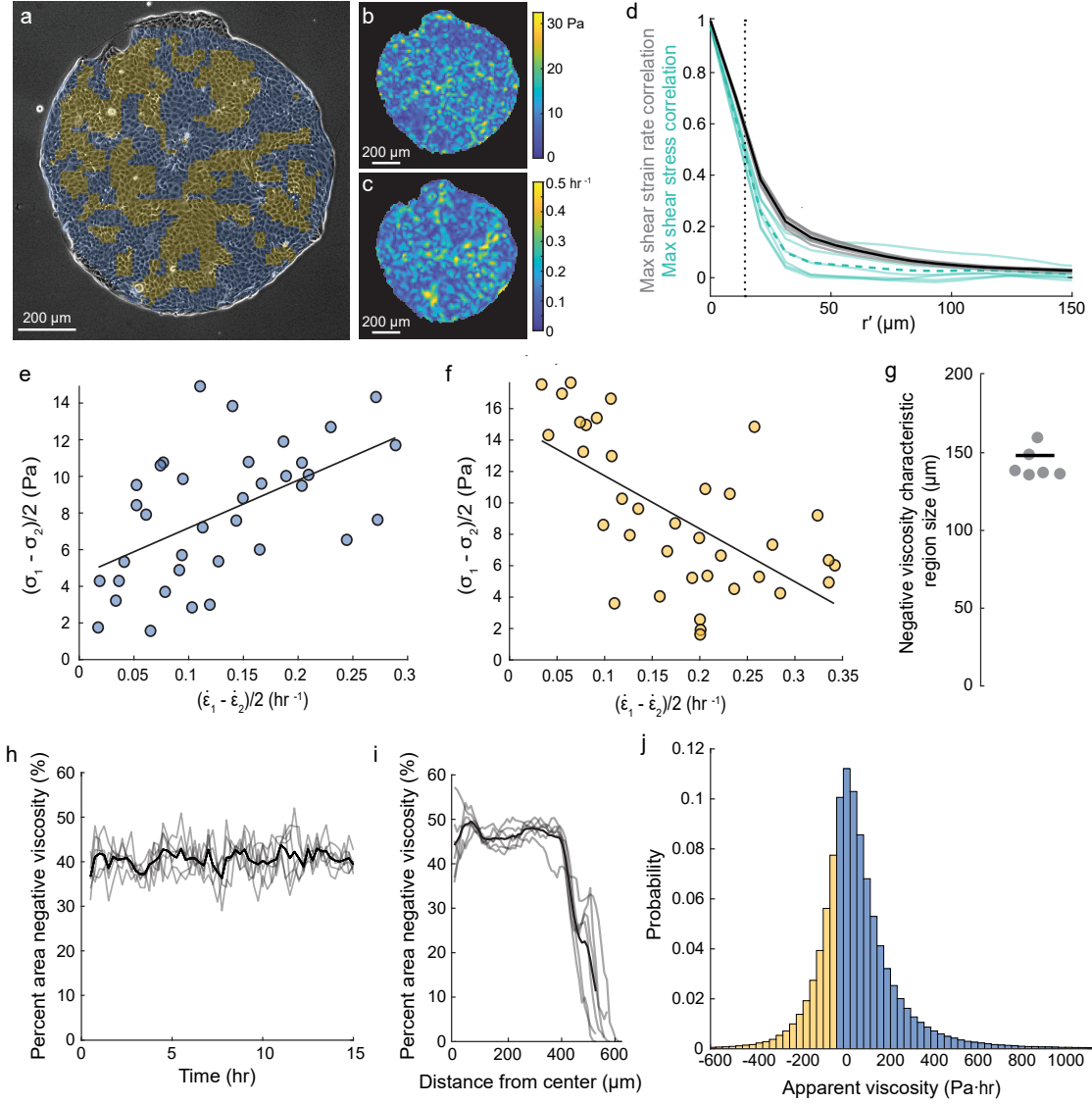


**Figure 1:** Viscosity in the cell monolayer. (a) Phase contrast image of cell monolayer overlaid with regions of positive (blue) and negative (yellow) viscosity. (b) Heat map of shear stress,  $(\sigma_1 - \sigma_2)/2$ . (c) Heat map of shear strain rate  $(\dot{\epsilon}_1 - \dot{\epsilon}_2)/2$ . (d) Spatial correlation of shear strain rate (gray) and shear stress (turquoise). The solid and dashed lines indicate averages of the respective spatial correlations; the dotted line indicates the size of a single cell. (e) Scatter plot of shear stress and shear strain rate within a representative window showing positive viscosity. (f) Scatter plot of shear stress and shear strain rate within a representative window showing negative viscosity. (g) Average size of regions of negative viscosity. (h) Percentage of the total island area exhibiting negative viscosity over time. (i) Percentage of the total island area exhibiting negative viscosity over distance from the center of the island. (j) Histogram showing apparent viscosity over 6 cell islands over 15 hr of imaging. In panels g–i, gray dots and gray lines are data from different cell monolayers; black lines indicate means.

To explore the temporal evolution of regions of negative viscosity, we measured the percentage of the total area within the cell island exhibiting negative viscosity over time, with results showing that for all times,  $\approx 40\%$  of the cell island exhibited negative viscosity (Fig. 1h). We also determined how negative viscosity depended on position, with the locations near the edge of the island tending to exhibit positive viscosity (Fig. 1i), possibly because cell stresses and tractions are systematically altered near boundaries.<sup>6</sup> To avoid possible artifacts associated with boundaries, we analyzed data in locations  $> 100 \mu\text{m}$  from the boundaries for the rest of our study. Finally, we plotted a histogram of the signed value of viscosity for all

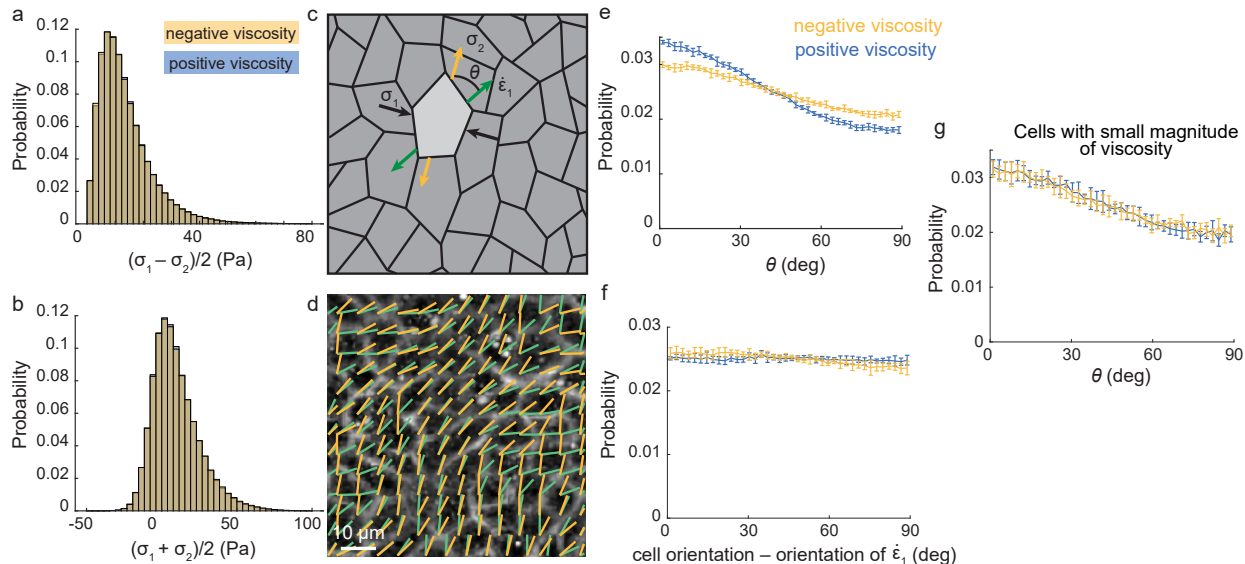


**Figure 2:** Negative viscosity due to alignment of the second principal stress and the first principal strain rate. (a) Histogram of  $(\sigma_1 - \sigma_2)/2$  in regions of positive and negative viscosity. (b) Histogram of  $(\sigma_1 + \sigma_2)/2$  in regions of positive and negative viscosity. (c) Depicts the stresses (black and yellow arrows) applied by a cell (light gray) onto its neighbors (dark gray). To produce negative viscosity, the orientation of the second principal stress,  $\sigma_2$ , must align with the orientation of the first principal strain rate,  $\dot{\epsilon}_1$  (green arrows). The difference between orientations of  $\sigma_2$  and  $\dot{\epsilon}_1$  is indicated by angle  $\theta$ . (d) Image of a negative viscosity region overlaid with lines depicting the orientations of  $\sigma_2$  (yellow) and  $\dot{\epsilon}_1$  (green). (e) Histogram of angle  $\theta$  between orientations of  $\sigma_2$  and  $\dot{\epsilon}_1$  in regions of negative and positive viscosity. (f) Histogram of the angle between cell orientation and the orientation of  $\dot{\epsilon}_1$ . (g) Histogram of  $\theta$  in cells with small magnitude of viscosity, defined as below the 10th percentile. All histograms are over 6 cell islands and 15 hr of imaging. Error bars represent the standard deviation of the probability values for each bin, calculated across all cell islands.

locations in 6 different cell islands, with results ranging from -600 to 800 Pa·hr and the distribution centered on values slightly greater than 0 (Fig. 1j).

Although a reduction in viscosity due to activity has been observed in other systems,<sup>20–24</sup> a distinction here is that the prior manuscripts measured the average viscosity of the system, whereas here the data quantify the apparent viscosity at every point in space. Importantly, the finding that negative viscosity occurs in regions spanning many cell widths indicates that the negative viscosity is unlikely to result from random fluctuations. Moreover, the regions of negative viscosity are not caused by individual cells or individual rearrangement events; rather, the data suggest the existence of a more complex intercellular coordination.

## B. Alignment of Stresses and Strain Rates Cause Negative Viscosity

To develop an explanation for how the viscosity could become negative, we next studied the stresses and strain rates more closely. We began by quantifying distributions of stresses in regions of positive and negative viscosity. The shear stress,  $(\sigma_1 - \sigma_2)/2$ , ranged from 0 to 80 Pa with no notable difference between distributions in regions of positive or negative viscosity (Fig. 2a). The average normal stress,  $(\sigma_1 + \sigma_2)/2$  had a nearly symmetric distribution shifted toward positive values, indicating a tendency for tensile (pulling) stresses, again with no difference between regions of positive and negative viscosity (Fig. 2b). Next, we considered the explanation from theories developed for active systems such as swimming bacteria and active nematic materials,<sup>18,19,25</sup> which showed that if activity creates pushing (extensile) stresses that locally align with the predominant orientation of extensile flow, the effective viscosity can be reduced and even become negative. In our system, the largest pushing (extensile) stress is the second principal stress  $\sigma_2$ . For  $\sigma_2$  to



propel the flow, it would have to align with the first principal strain rate  $\dot{\epsilon}_1$  (Fig. 2c). Thus, we plotted orientations of  $\sigma_2$  and  $\dot{\epsilon}_1$  in a representative field of view, with results qualitatively showing a tendency for alignment (Fig. 2d). To quantify the alignment, we plotted histograms of angle  $\theta$  between  $\sigma_2$  and  $\dot{\epsilon}_1$ . Although slight, the histograms exhibited a peak at zero, indicating a tendency for alignment between  $\sigma_2$  and  $\dot{\epsilon}_1$  (Fig. 2e). Importantly, the peak at zero was statistically meaningful, as the variability in the histograms between different islands was negligible (Fig. 2e). Surprisingly, the tendency for alignment was greater for regions of positive viscosity compared to negative. To investigate further, we considered the recent finding that both extensile and contractile behavior occur within the same cell island,<sup>26</sup> where “contractile” refers to cells whose body tends to align with the orientation of maximal principal stress,  $\sigma_1$ , and, “extensile,” cells that align with the orientation of  $\sigma_2$ . Histograms for only contractile and only extensile cells showed no differences (Appendix C, Fig. 9). Next, we studied the angle between  $\dot{\epsilon}_1$  and the cell body by plotting a histogram. The data were almost uniformly distributed for cells in regions of positive viscosity, but had a slight peak at zero for cells in regions of negative viscosity, indicating a slight tendency for these cells to align with the flow (Fig. 2f). We next asked whether the tendency for alignment between cell stresses and the flow depended on cell aspect ratio. We identified elongated cells (see Methods) and plotted histograms of angle  $\theta$ , which showed an approximately equal tendency toward zero for cells in regions of positive and negative viscosity (Appendix C, Fig. 9).

To investigate further, we reasoned that negative viscosity indicates injection of energy into the flow, meaning that the alignment between  $\sigma_2$  and  $\dot{\epsilon}_1$  could depend on how much energy is injected into the flow, or, equivalently, the distribution of  $\theta$  could depend on the magnitude of viscosity. To this end, we defined a threshold by the 10th percentile of viscosity magnitude, and analyzed data for all cells having viscosity magnitude below this threshold. For the thresholded data, the distribution of angle between  $\sigma_2$  and  $\dot{\epsilon}_1$  retained the peak at 0, and the difference between distributions for cells of negative and positive viscosity disappeared (Fig. 2g). Hence, the tendency for alignment between cell stresses and the flow was strongest for cells that dissipate energy (positive viscosity) or inject small amounts of energy (negative viscosity with small magnitude). Cells injecting the largest amounts of energy into the flow (negative viscosity with large magnitude) exhibited reduced alignment with the flow.

### C. Negative Viscosity is Robust to Perturbations to Stresses and Flow Rates

Next, we asked whether we could perturb the fraction of cells exhibiting negative viscosity by increasing or decreasing activity in the cell monolayer. We used two treatments, CN03 and cytochalasin D, which increase and decrease force generation, respectively.<sup>15</sup> In these experiments, we imaged the cell islands in control conditions for 1 hr, then treated with vehicle control, CN03, or cytochalasin D and imaged for an additional 14 hr. Representative images of shear stress and strain rate at 1.5 hr after treatment are shown in Fig. 3a. Results from multiple different experiments showed that CN03 increased the shear stress and strain rate by factors of approximately 2 and 1.5, respectively, whereas cytochalasin D decreased the shear stress and strain rate by approximately 20% and 50%, respectively (Fig. 3b, c).

Next, we determined locations in the cell islands having positive and negative viscosity at each time point under the CN03 and cytochalasin D treatment (Fig. 3a). We also plotted histograms of  $\theta$ , the angle difference between the second principal stress and first principal strain rate. The results were similar to control conditions (Fig. 1e), namely there was a slight tendency of  $\theta$  toward zero (Appendix C, Fig. 10). We then quantified the fraction of area having negative viscosity. Despite the notable changes in stress and strain rate caused by the treatments, the fraction of the island area having negative viscosity was unchanged by the treatments, being approximately 40% of the cell monolayer in all conditions (Fig. 3d).

Following the observation that the fraction of the cells exhibiting negative viscosity was unaffected by

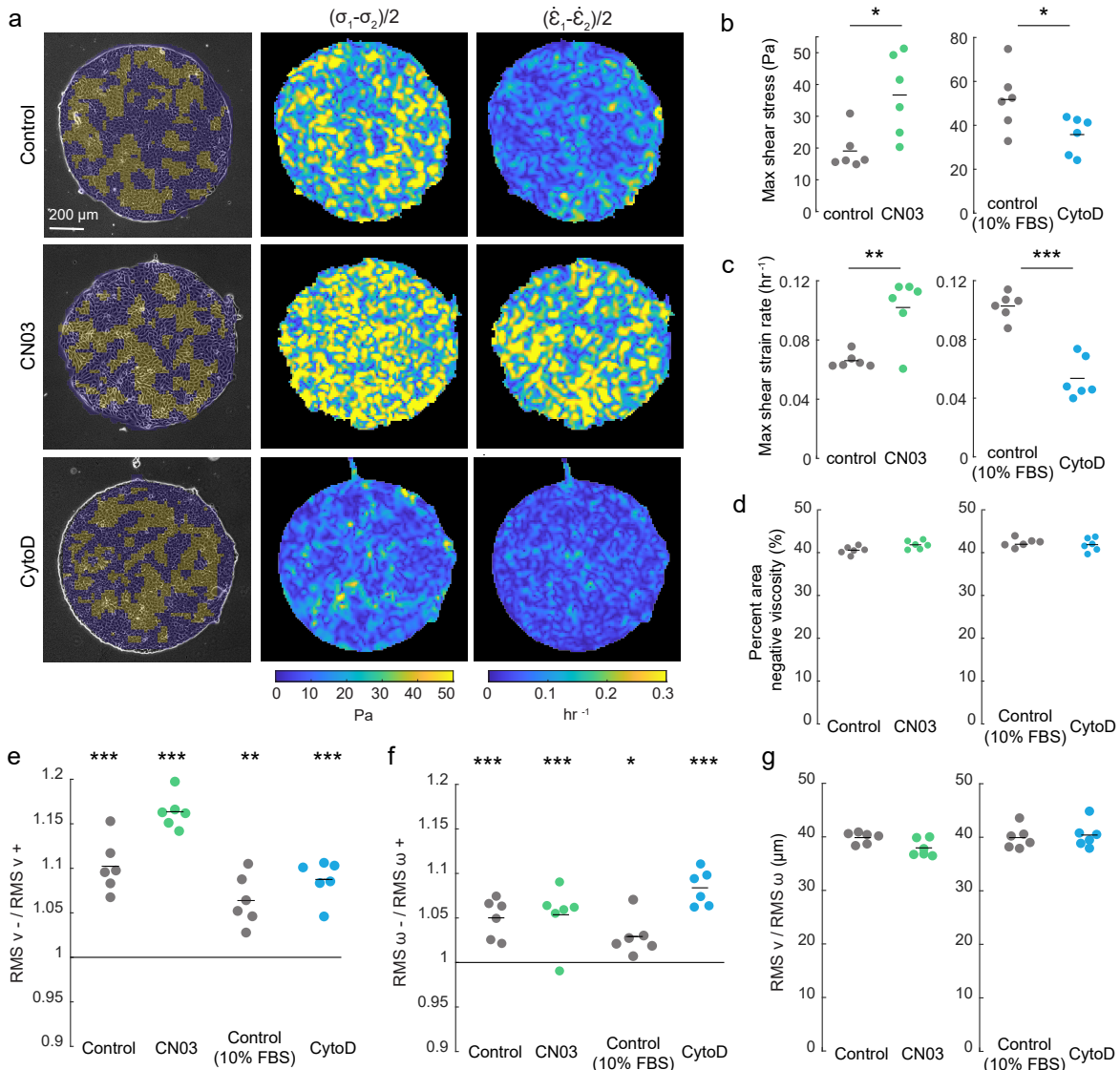


**Figure 3:** Altering stresses and flow rates does not alter the fraction of cells with negative viscosity. (a) Phase contrast image of a cell monolayer (left) overlaid with regions of positive (blue) and negative (yellow) viscosity. Heat maps of maximum shear stress (center) and maximum shear strain rate (right). Data are shown for control cells (top row) and cells treated with CN03 (middle row) and cytochalasin D (cytoD, bottom row). (b) Shear stress for treatments and their respective vehicle controls. (CN03  $p = 0.012$ , cytoD  $p = 0.039$ , two-sample t-tests). As described in methods, the control for cytochalasin D used a higher concentration of FBS, 10%. (c) Shear strain rate for treatments and their respective vehicle controls (CN03  $p = 0.002$ , cytoD  $p < 0.0001$ , two-sample t-tests). (d) Percent negative viscosity within the monolayer for control and treatment cases (CN03  $p = 0.5$ , cytoD  $p = 0.99$ , two sample t-tests). (e) Ratio of RMS velocity in regions of negative viscosity to positive viscosity for control and treatment cases (control  $p < 0.0001$ , CN03  $p < 0.0001$ , control 10% serum  $p = 0.002$ , cytoD  $p < 0.0001$ , one-sample t-tests in comparison to 1). (f) Ratio of RMS vorticity,  $\omega$ , in regions of negative viscosity to positive viscosity for control and treatment cases (control  $p < 0.0001$ , CN03  $p < 0.0001$ , control 10% serum  $p = 0.02$ , cytoD  $p < 0.0001$ , one-sample t-tests in comparison to 1). (g) Characteristic size of a vortex, given by  $\text{RMS } v / \text{RMS } \omega$ , for the control and treatment cases (CN03  $p = 0.11$ , cytoD  $p = 0.09$ , two sample t-tests). For all panels, a dot indicates the mean of a cell island over time, and black bars indicate means.

increasing or decreasing stresses and strain rates, we considered how negative viscosity affected the cell flow. We predicted that, given negative viscosity injects energy into the flow, cells in regions of negative viscosity would move faster compared to cells in regions of positive viscosity. To begin, we ruled out an alternative explanation that, in regions of negative viscosity, energy injected via cell-substrate traction might be reduced (Appendix B and Appendix C, Fig. 11). Next, we computed the root-mean-square (RMS) of cell velocity in regions of negative and positive velocity and took the ratio. Results indicated that in all

conditions, the average ratio was  $> 1$ , typically in the range of 1.05–1.2 (Fig. 3e). Hence, in regions of negative viscosity, cells move faster than in regions of positive viscosity. Current understanding is that viscous energy dissipation at the substrate is proportional to velocity,<sup>8,13,14,27–30</sup> meaning for cells that inject energy via negative viscosity, that surplus energy is likely dissipated at the cell-substrate interface.

We also studied the vorticity  $\omega$  in regions of negative and positive viscosity, with results being similar, namely vorticity was elevated in regions of negative viscosity (Fig. 3f). Finally, wondering whether negative viscosity is related to the common observation of rotational eddies in the cell monolayer reminiscent of turbulence,<sup>1–3</sup> we quantified the characteristic size of a turbulent eddy by computing the ratio of the RMS of velocity divided by the RMS of vorticity. This analysis resulted in a characteristic size of approximately 40  $\mu\text{m}$  under all conditions (Fig. 3g), which is similar to a prior study<sup>31</sup> but substantially different than the typical size of a region having negative viscosity ( $\approx 150 \mu\text{m}$ , Fig. 1g), suggesting that our observation of negative viscosity is distinct from the common observation of turbulent-like rotation within the flow.

#### D. Source of Energy for Negative Viscosity

The injection of energy via negative viscosity, combined with the observation of faster cell speeds in regions of negative viscosity, raise the question of whether cells in regions of negative viscosity produce energy at an elevated rate. We used fluorescent imaging of glucose uptake, via (2-(N-(7-Nitrobenz-2-oxa-1,3-diazol-4-yl)Amino)-2-Deoxyglucose (2-NBDG), and mitochondrial membrane potential, via Tetramethylrhodamine, Ethyl Ester, Perchlorate (TMRE), both of which are markers of metabolic activity<sup>32–34</sup> (Fig. 4a, b). To quantify the results, we determined the average fluorescent intensity in regions of negative and positive viscosity, and computed the ratio for multiple different cell islands. The data consistently showed that regions of negative viscosity displayed both elevated glucose uptake and elevated mitochondrial membrane potential (Fig. 4c), indicating increased metabolic activity in regions of negative viscosity. Following our prior measurement that a region of negative viscosity has characteristic size of 149  $\mu\text{m}$  (Fig. 1g), we also computed spatial autocorrelations of the images of both glucose uptake mitochondrial membrane potential (Fig. 4d). The autocorrelations decayed sharply within the first 20  $\mu\text{m}$ , which is due to the fluorescent imaging clearly defining the cell outlines (Fig. 4a, b insets). After the first 20  $\mu\text{m}$ , the decay was slower, indicating that glucose uptake and mitochondrial membrane potential are spatially correlated, possibly due to intercellular coordination. The spatial correlation lengths of glucose uptake and mitochondrial membrane potential were 166 and 114  $\mu\text{m}$ , which is close to the characteristic size of a region of negative viscosity ( $\approx 150 \mu\text{m}$ , Fig. 1g).

The closely matched sizes of regions of elevated metabolism and negative viscosity suggest that metabolism may be the underlying cause of negative viscosity, which raises the possibility that cells having surplus energy inject it into the flow using negative viscosity. Before testing this hypothesis, we first ruled out an alternative explanation based on substrate-to-cell tractions, showing that cells with elevated metabolism do not inject energy into the cell layer via tractions (Appendix B, Appendix C, Fig. 12). Next, as a first test of our hypothesis, we imaged the cells over time before and after inhibiting metabolism. Both oxidative phosphorylation and glycolysis were inhibited, using NaCN and 2-Deoxy-d-glucose (2-DG), respectively. The two metabolic pathways were inhibited simultaneously to prevent, as much as possible, compensatory effects wherein inhibiting one pathway leads to compensation by the other. Importantly, under this treatment, metabolic activity decreased, but the cells were alive over the entire time course of our experiment, as indicated by the cell stresses and strain rates, which never reached zero (Appendix C, Fig. 13). To quantify the effects of inhibiting metabolism on negative viscosity, for each cell island, we computed the area having negative viscosity at all time points and then normalized by the average area for time points before inhibition. In control experiments, the normalized area of negative viscosity was unchanged, maintaining a value of unity. By contrast, for cell islands with metabolism inhibited, the normalized area of negative vis-

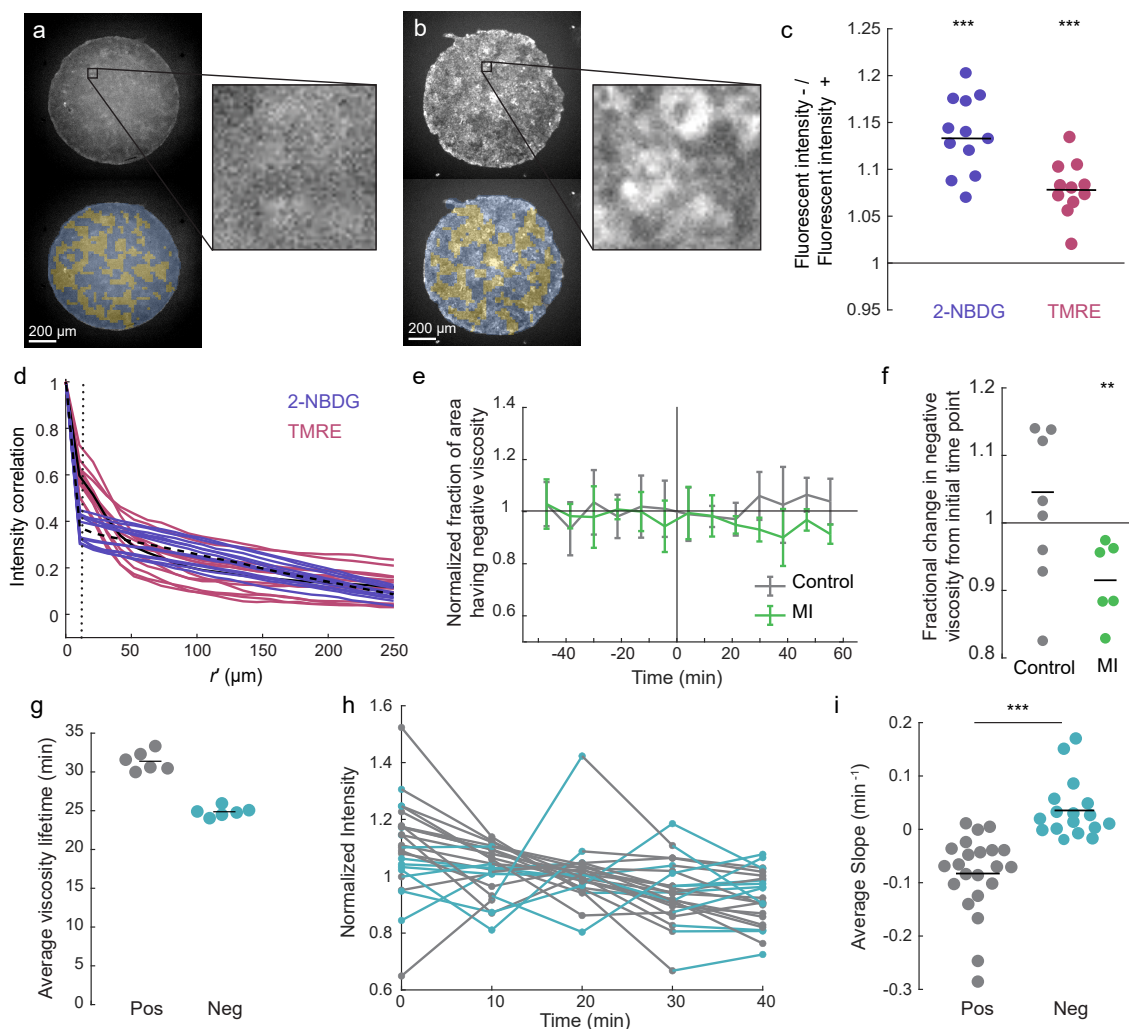


**Figure 4:** Regions of negative viscosity are more metabolically active. (a) Fluorescent image of cell island stained with 2-NBDG (top) and overlaid with map depicting positive (blue) and negative (yellow) viscosity (bottom). The black box is an enlarged view, showing the outlines of individual cells. (b) Fluorescent image of cell island stained with TMRE (top) and overlaid with map depicting positive (blue) and negative (yellow) viscosity (bottom). The black box is an enlarged view, showing the outlines of individual cells. (c) Ratio of 2-NBDG and TMRE fluorescent intensity in regions of negative viscosity (2-NBDG  $p < 0.0001$ , TMRE  $p = p < 0.0001$ , one-sample t-tests in comparison to 1). (d) Spatial correlation of TMRE and 2-NBDG fluorescent intensity. The dotted line indicates the size of a single cell. (e) Normalized fraction of area having negative viscosity before and after MI. All values were normalized by the mean of times  $\in (-50, 0)$  min. The metabolic inhibition occurred at  $t = 0$  min. Lines represent the mean and error bars represent the standard deviation. (f) Fractional change in area of negative viscosity from initial time point to last time point (Control  $p = 0.396$ , MI  $p = 0.004$ , one-sample t-test in comparison to 1). (g) Average lifetime of regions of positive and negative viscosity. (h) Fluorescent intensity of TMRE over time. Each line indicates a randomly chosen  $62 \times 62 \mu\text{m}^2$  ROI. Gray and blue line segments indicate times over which the ROI has positive and negative viscosity, respectively. Fluorescent intensity in each ROI was normalized by the mean over all time points in that ROI. (i) Average slope of normalized fluorescent intensity for positive and negative viscosity line segments of each ROI ( $p < 0.0001$ , paired sample t-test). Dots in panels c, f, and g indicate averages over a cell island. Black bars indicate means.

cosity decreased approximately 30 min following the inhibition (Fig. 4e). To quantify these results further, we averaged the normalized area of negative viscosity for all time points  $> 30$  min after treatment (chosen because it takes this long for the treatment to take effect in this cell type<sup>35</sup>). Whereas the fraction of cells having negative viscosity was unchanged in control conditions, the metabolic inhibition reduced the fraction of cells having negative viscosity by approximately 10% (Fig. 4f). Hence, inhibiting metabolism reduced the fraction of cells exhibiting negative viscosity.

To test further the hypothesis that elevated metabolism causes negative viscosity, we considered how both negative viscosity and metabolism vary over time. We first quantified the typical lifetime of regions of positive and negative viscosity, which averaged 32 and 25 min, respectively (Fig. 4g). We then performed an experiment to image metabolism over time periods longer than this characteristic time. The fluorescent indicators of metabolism photobleach quickly, especially 2-NBDG, which photobleached too quickly for time lapse imaging. Fortunately, the imaging of mitochondrial membrane potential by TMRE was relatively stable when imaging every 10 min for 40 min, which is slightly longer than the characteristic lifetimes of regions of positive and negative viscosity. We analyzed  $62 \times 62 \mu\text{m}^2$  regions of interest (ROIs), which were chosen randomly from 6 different islands. In each ROI, we quantified the average fluorescent intensity and determined whether the viscosity was negative or positive. We normalized the fluorescent intensity by the average for all time points and plotted the normalized intensity over time, with line color indicating positive or negative viscosity. The common trend in the data was that when the mitochondrial membrane potential decreased over time, the viscosity was positive, and when membrane potential increased over time, the viscosity was negative (Fig. 4h and Appendix C, Fig. 14). To quantify this relationship, for the data in ROIs shown in Fig. 4h, we calculated the slope of each line segment in each 10 min time window between imaging. In each ROI, the slopes of all line segments in time windows corresponding to positive viscosity in that ROI were averaged, as were the slopes of all line segments corresponding to negative viscosity. The averaged slopes were then plotted for positive and negative viscosity, with results showing that slopes during periods of negative viscosity were significantly larger than those during periods of positive viscosity (Fig. 4i). Hence, these data indicate a temporal correlation, wherein increases in mitochondrial membrane potential tend to occur concurrently with negative viscosity. Together, these data suggest that negative viscosity may be a mechanism whereby cells that have surplus energy available inject that excess energy into the flow.

### III. DISCUSSION

Motivated by the fact that the energy injected by cells must be dissipated by viscous processes, we developed a method to quantify the effective viscosity over space and time within an epithelial cell monolayer. Surprisingly, the results revealed regions of negative viscosity, which were caused not by the magnitudes of stresses but rather by the alignment, namely, the orientation of second principal stress aligns with the first principal strain rate. Although this physical mechanism has been proposed before,<sup>18,19,25</sup> prior experiments in other systems quantified stresses and flows but not their orientations,<sup>20–24</sup> meaning the prior experimental verification of this mechanism was indirect. Here, we give a direct experimental verification of the physical mechanism for negative viscosity. Interestingly, our direct experimental verification has also revealed that, although cells tend to align their stresses so as to propel the flow, the cells injecting the most energy into the flow are less aligned, which may be a mechanism whereby the cells doing the most work on the flow realign slightly to reduce their workload.

An advantage of our experiments that quantified viscosity in both space in time is that the data showed that regions of negative viscosity are correlated in space, with a characteristic size of approximately 150  $\mu\text{m}$ . These regions coincided with regions of elevated cellular metabolism, suggesting that cells having surplus energy may inject that energy into the flow via negative viscosity. Some prior models have used a negative viscosity term,<sup>36,37</sup> which was intended as a simplified means of injecting energy into the system. Our observation of negative viscosity shows that a model using negative viscosity is, in fact, a physically accurate description of an epithelial cell monolayer. One point to emphasize, however, is that our data, especially the data showing negative viscosity coincides with elevated metabolism, show that any modeling approach should inject energy in spatial regions of characteristic size matching those measured here.

Interestingly, the fraction of the cell layer exhibiting negative viscosity was  $\approx 40\%$  for nearly all experi-

mental conditions, even under treatments that substantially increased and decreased stresses and strain rates. This observation hints that there may be some underlying mechanism for achieving such robust behavior. It is reasonable to suspect that mechanism for robustness may be cellular metabolism, which results from a highly complex network of interactions that create compensatory mechanisms which enable the cell to maintain a consistent metabolic activity.<sup>38–40</sup> Consistent with this reasoning, only the treatment that directly inhibited metabolism had an effect on the fraction of cells exhibiting negative viscosity. It appears, then, that it may have been evolutionarily favorable for cells to leverage negative viscosity as a means to inject surplus energy into the collectively flowing monolayer. Implications of this finding could be far reaching. In metastasis, for example, cancer cells often have altered metabolic activity,<sup>41,42</sup> which raises the questions of whether and how negative viscosity affects cancer cell invasion. It also may be the case that negative viscosity is a favorable means of injecting energy into other active systems, in which case negative viscosity could be a valuable design principle for efforts to create active materials with desired properties.

## **IV. METHODS**

### **A. Cell culture**

Madin-Darby Canine Kidney (MDCK) type II cells were maintained in low-glucose Dulbecco's modified Eagle's medium (DMEM, 10-014, Corning) supplemented with 10% fetal bovine serum (FBS, Corning) and 1% Penicillin-Streptomycin (Corning). Human keratinocytes (HaCaTs) were maintained in Dulbecco's modified Eagle's medium (DMEM, 10-013, Corning) supplemented with 10% fetal bovine serum (FBS, Corning) and 1% Penicillin-Streptomycin (Corning). Cells were maintained at 37°C and 5% CO<sub>2</sub>. Unless otherwise stated, cells were moved to medium containing 2% FBS 8 hr before the start of the experiment.

### **B. Chemical treatments**

Cells were treated with 0.05 μM cytochalasin D (Sigma) and 2 μg/mL CN03 (Cytoskeleton Inc.). Stock solutions were made by dissolving cytochalasin D in dimethylsulfoxide and CN03 in water, as in our previous work.<sup>43</sup> The stock solutions were diluted in 1× phosphate buffered saline to the desired concentrations. Medium containing 10% FBS was used for the cytochalasin D experiments (for both the control and treated groups) in order to establish a higher baseline of cellular contraction, which ensured that the decrease in contraction upon treatment would be measurable.

### **C. Cell seeding and optical microscopy**

Polyacrylamide (PA) gels of 6 kPa Young's modulus embedded with fluorescent particles and patterned with 1 mm diameter circles were prepared using methods previously described.<sup>14,15</sup> Briefly, 1 mm circular holes were punched into polydimethylsiloxane sheets, which were adhered to the PA gels. The holes were then coated in 0.1 mg/mL type I rat tail collagen (BD Biosciences) with the covalent crosslinker sulfo-SANPAH (50 mg/mL, Pierce Biotechnology). MDCK cells were seeded onto the masks, allowed to adhere for 1 hr, and the masks were removed. Cells were cultured to confluence overnight. For time lapse imaging, cell islands and fluorescent particles were imaged every 15 min for 15 hr. For metabolism (TMRE, 2-NDBG), and metabolic inhibition imaging, cells and fluorescent particles were imaged every 10 min for 1 or 2 hr, respectively. All imaging was performed on an Eclipse Ti-E microscope (Nikon Instruments) with a 10× numerical aperture 0.5 objective (Nikon) and an Orca Flash 4.0 digital camera (Hamamatsu) using Elements Ar software (Nikon). Imaging was performed at 37°C and 5% CO<sub>2</sub>. After imaging, cells were removed by incubating in 0.05% trypsin, and images of a traction-free reference state was collected.

#### D. Image correlation, traction force microscopy, monolayer stress microscopy, and cell aspect ratio

To compute cell-induced substrate displacements, Fast Iterative Digital Image Correlation (FIDIC)<sup>44</sup> was performed using  $64 \times 64$  pixel subsets, with a spacing of 16 pixels (10.4  $\mu\text{m}$ ). Cell-substrate tractions were computed using Fourier Transform Traction Cytometry<sup>45</sup> with corrections for the finite substrate thickness.<sup>4,46</sup> Stresses within the monolayer were computed using Monolayer Stress Microscopy<sup>5,16,17</sup> which employs the principle of force equilibrium to the cell-substrate tractions, yielding the stress tensor in the plane of the cell layer. The maximal and minimal eigenvalues of the stress tensor are the first and second principal stresses,  $\sigma_1$  and  $\sigma_2$ , respectively, in which tensile (pulling) stress is positive, and compressive (pushing) stress is negative.

Cell velocities,  $\vec{v}$ , were computed using incremental FIDIC using the same subset and spacing as described above. The strain rate tensor  $\dot{\epsilon}$  was calculated according to  $\dot{\epsilon} = [\nabla\vec{v} + (\nabla\vec{v})^T]/2$  with  $\nabla\vec{v}$  being the velocity gradient tensor and  $(\cdot)^T$  indicating the transpose. The maximal and minimal eigenvalues of the strain rate tensor are the first and second principal strain rates,  $\dot{\epsilon}_1$  and  $\dot{\epsilon}_2$ , respectively.

The shear stress was computed by taking  $(\sigma_1 - \sigma_2)/2$ , and the shear strain rate was computed by taking  $(\dot{\epsilon}_1 - \dot{\epsilon}_2)/2$ . To compute the viscosity within local regions, a moving window was utilized (window size described in Appendix C, Fig. S2). Within each window, the ratio of shear stress to the shear strain rate was taken, with a linear fitted slope yielding the viscosity. In considering the window size used for the calculation of viscosity, we aimed to balance computational efficiency with a need for a sufficiently large window to satisfy treating the monolayer as a continuum while maintaining a small enough window to discern spatial patterns. We chose the  $62 \times 62 \mu\text{m}^2$  window as it was the largest window size that does not substantially smooth the data and large enough to satisfy continuum conditions. Therefore, to optimize computational efficiency while ensuring a continuum approach, a  $62 \times 62 \mu\text{m}^2$  window was selected.

Cell orientation was computed using the ImageJ plugin OrientationJ<sup>47</sup> on phase contrast images of the monolayer. A window size of 16 pixels (10.4  $\mu\text{m}$ ) was used, and the ‘‘Cubic Spline’’ option for computing the gradient was used. Elongated cells were identified by taking regions in the top 10% of the coherency.

#### E. Spatial correlations

Spatial correlations of scalar quantities  $u$  were computed according to

$$C(r') = \frac{\sum \bar{u}(\vec{r})\bar{u}(\vec{r} + \vec{r}')}{\sum \bar{u}^2(\vec{r})} \quad (1)$$

where  $C$  is the spatial correlation,  $\bar{u} = u - u_m$  where  $u_m$  is the mean of  $u$ ,  $\vec{r}$  and  $\vec{r}'$  are position vectors, and  $r' = |\vec{r}'|$ . The sums were calculated over all positions,  $\vec{r}$ . The correlation length was defined as the value of which the spatial correlation decayed to a value of 0.2, which is the same value used in prior studies.<sup>43,48</sup>

#### F. Metabolic imaging and inhibition

Mitochondrial membrane potential was measured by incubating the cell islands for 30 min in medium (DMEM supplemented with 2% FBS, as stated above) containing 25  $\mu\text{M}$  TMRE (Thermo). After incubation, the medium was replaced with TMRE-free medium, and the islands were imaged. Glucose uptake was measured by incubating cell islands for 1 hr in 400  $\mu\text{M}$  2-NBDG (Thermo) suspended in medium that had no FBS or glucose (DMEM, no glucose, Thermo). Following the incubation, the medium was replaced with medium having no 2-NBDG, FBS, or glucose, and the islands were imaged. Due to the tendency for these dyes to photobleach, the ImageJ ‘‘Bleach Correction’’ function was used to correct images, using the ‘‘histogram matching’’ method.



Metabolic inhibition experiments were performed on cell islands in a solution containing 135 mM NaCl, 5 mM KCl, 1.5 mM KCl<sub>2</sub>, 1 mM MgSO<sub>4</sub>, 10 mM HEPES, and 5.5 mM glucose. Metabolic inhibition was initiated with a spike of 10 mM 2-Deoxy-D-glucose (2-DG), and 2.5 mM NaCN to the solution.<sup>35,49</sup>

### **G. Statistical testing**

Statistical analysis between groups was done using a Student's t-test and statistical analysis within the same group was done using a one-sample t-test. For all tests, a sample size of at least  $n = 5$  was used. Comparisons between more than two groups used one-way ANOVA followed by a Tukey Honest Significant Difference test for pair-wise comparisons. A value of  $p < 0.05$  was considered statistically significant, with \*, \*\*, and \*\*\* indicating  $p < 0.05$ ,  $p < 0.01$ , and  $p < 0.001$ , respectively.

### **Acknowledgments**

We thank Christian Franck, Melissa Skala, Saverio Spagnolie, and Thomas Chandler for valuable suggestions and feedback. This work was supported by NSF grant CMMI-2205141 and NIH grant R35GM151171.

### **Code Availability**

Code used to analyze experimental data is available at <https://github.com/jknotbohm/FIDIC> and <https://github.com/jknotbohm/Cell-Traction-Stress>.

### **Ethics declarations**

The authors declare no competing interests.

## Appendices

### Appendix A: Cell-substrate tractions in regions of positive and negative viscosity.

In considering that negative viscosity is a mechanism for injection of energy by the cells into the flow via stresses within the monolayer, we considered a second potential mechanism for energy injection, namely the tractions at the cell-substrate interface, which can have strong effects on the collective motion, such as by tuning the overall fluidity of the cell layer.<sup>15,50</sup> One possibility is that, because negative viscosity injects energy into the cell layer, less energy injection by traction is required, in which case tractions would be smaller in regions of negative viscosity. To test this possibility, we quantified the root-mean-square of tractions in regions of negative and positive viscosity and computed the ratio for multiple different cell islands. In control conditions and islands treated with cytochalasin D, the ratio was not statistically different from unity. In cell islands treated with CN03, the ratio was slightly above unity, indicating that some cases, tractions are elevated, rather than reduced in regions of negative viscosity (Appendix C, Fig. 11a). Next, we considered that for the cell-substrate traction to inject energy, the traction (applied by the substrate to the cells) would have to point in the same direction as the cell velocity. We, therefore, measured the angle  $\phi$  between substrate-to-cell traction and velocity in multiple cell islands. Distributions were broad with peaks at both  $0^\circ$  and  $180^\circ$  (Appendix C, Fig. 11). The peaks at  $0^\circ$  indicate alignment between traction and velocity, meaning for those cells, traction injected energy into the system. Interestingly, the peak at  $0^\circ$  was more pronounced for cells exhibiting negative viscosity compared to positive (Appendix C, Fig. 11), indicating that cells with negative viscosity inject greater energy through tractions than those with positive viscosity. These data rule out the idea that tractions inject less energy in regions of negative viscosity.

### Appendix B: Cell-substrate tractions in regions of high and low metabolism.

The increased metabolic activity in regions of negative viscosity suggests that negative viscosity is a mechanism wherein cells that have surplus energy available can inject that excess energy into the flow. We also considered that there may be other mechanisms for cells with excess energy to inject that energy into the flow. The only other potential mechanism for energy injection is the cell-substrate tractions. For the cell tractions to propel the flow, the tractions applied by the substrate to the cell would have to point in the same direction as the cell's velocity. With this in mind, we calculated angle  $\phi$  between traction and velocity. The metabolic activity was no different in regions of propulsive traction ( $\phi < 90^\circ$ ) or resisting traction ( $\phi > 90^\circ$ ) (Appendix C, Fig. 12), indicating that the cell-substrate tractions are not a mechanism for injection of surplus energy into the flow.

## Appendix C: Supplemental Figures

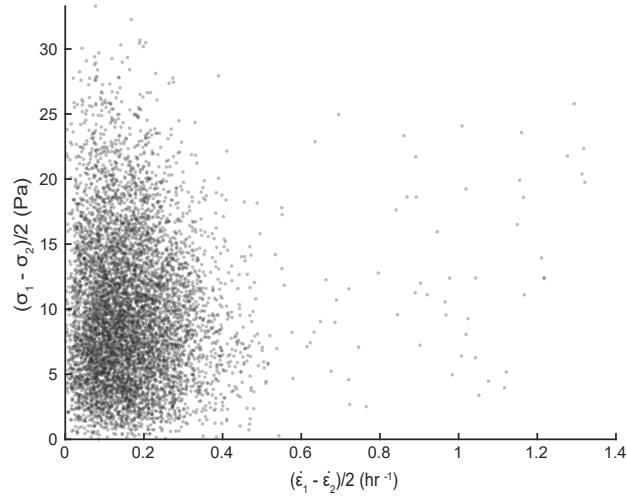


**Figure 5:** Shear stress and shear strain rate across the entire island is uncorrelated. The representative scatter plot shows  $(\sigma_1 - \sigma_2)/2$  against  $(\dot{\epsilon}_1 - \dot{\epsilon}_2)/2$  across an entire cell island at one point in time.

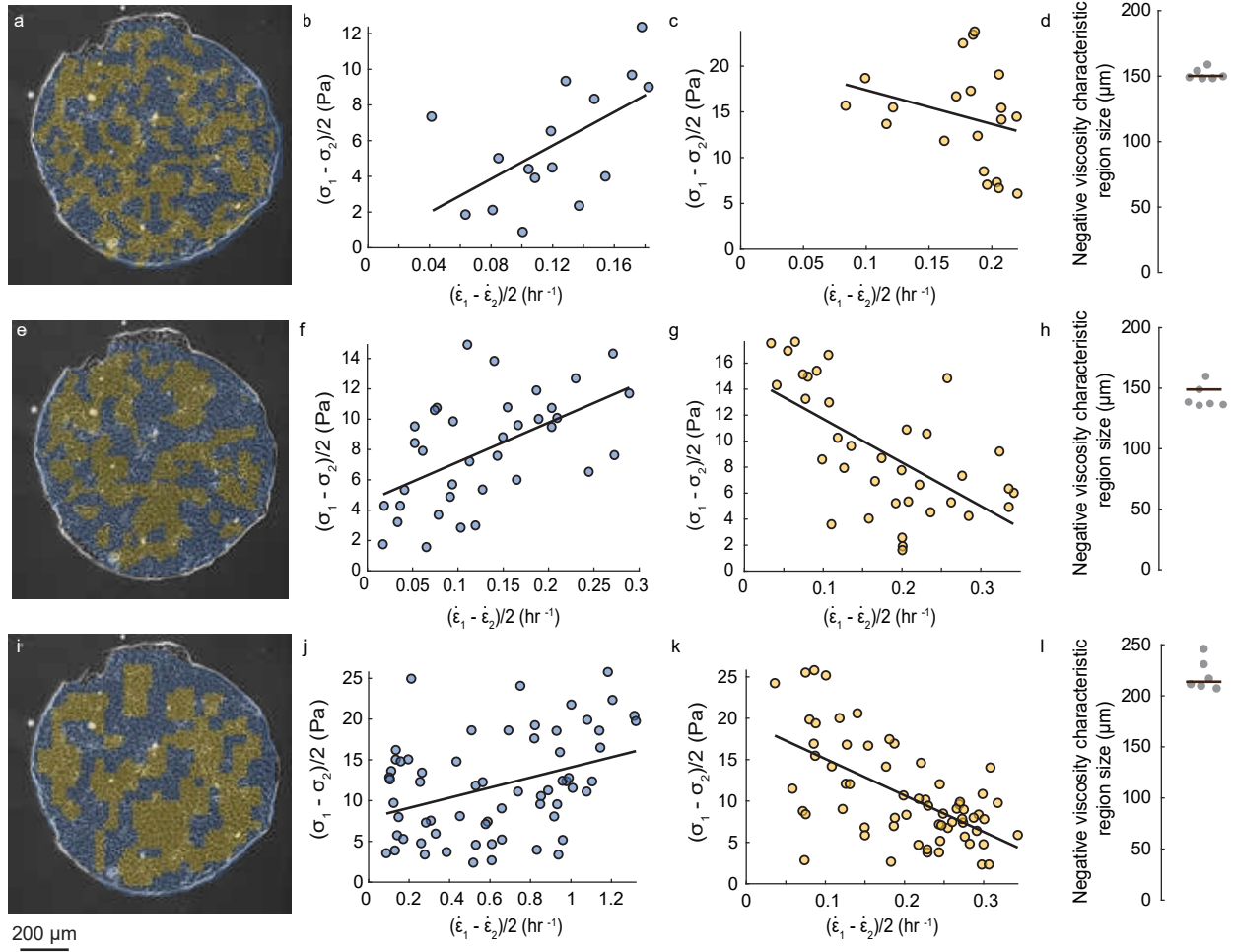


**Figure 6:** Observation of negative viscosity is insensitive to window size. (a) Phase contrast image of cell monolayer overlaid with regions of positive (blue) and negative (yellow) viscosity for a  $42 \times 42 \mu\text{m}^2$  window. (b) Scatter plot of shear stress and shear strain rate within a representative  $42 \times 42 \mu\text{m}^2$  window showing positive viscosity. (c) Scatter plot of shear stress and shear strain rate within a representative  $42 \times 42 \mu\text{m}^2$  window showing negative viscosity. (d) Characteristic size of regions of negative viscosity using  $42 \times 42 \mu\text{m}^2$  windows. The dots represent different cell islands and the black bar indicates the mean. Panels (e-h) and (i-l) repeat the analysis for  $62 \times 62 \mu\text{m}^2$  and  $84 \times 84 \mu\text{m}^2$  windows, respectively. The fact that the average size of a region of negative viscosity is similar for  $42 \times 42 \mu\text{m}^2$  and  $62 \times 62 \mu\text{m}^2$  windows indicates that the use of the  $62 \times 62 \mu\text{m}^2$  window, as in the main text, does not substantially smooth the data.

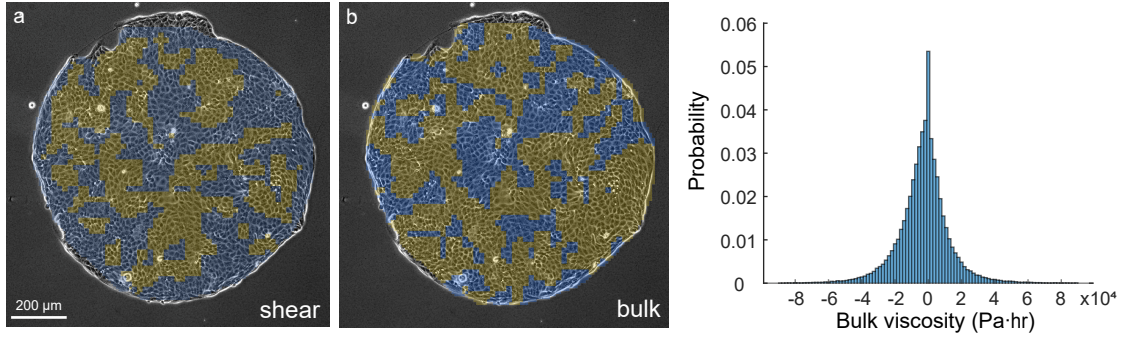


**Figure 7:** Bulk viscosity in the cell monolayer. (a) Image of a cell island overlaid with regions of positive (blue) and negative (yellow) shear viscosity. (b) Image of a cell island overlaid with regions of positive (blue) and negative (blue) bulk viscosity. (c) Histogram showing distribution of values of bulk viscosity from 6 cell islands over 15 hr of imaging.

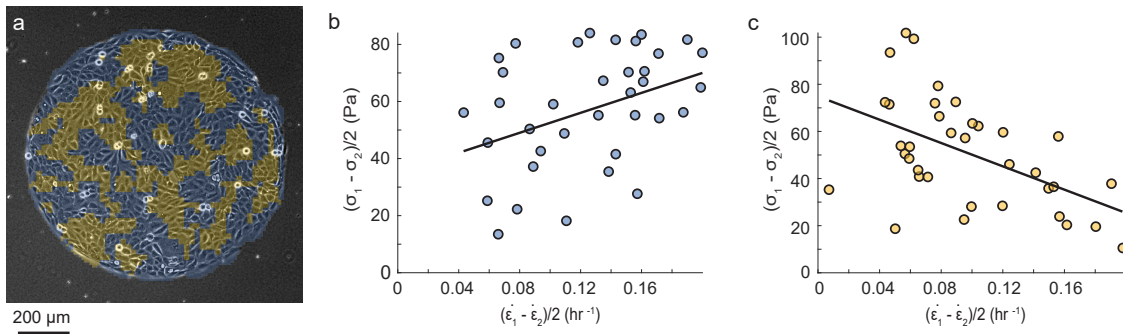


**Figure 8:** Negative viscosity is present in multiple cell types. (a) Phase contrast image of a HaCaT cell island overlaid with regions of positive (blue) and negative (yellow) viscosity. (b) Scatter plot of shear stress and shear strain rate within a representative window showing positive viscosity. (c) Scatter plot of shear stress and shear strain rate within a representative window showing negative viscosity.

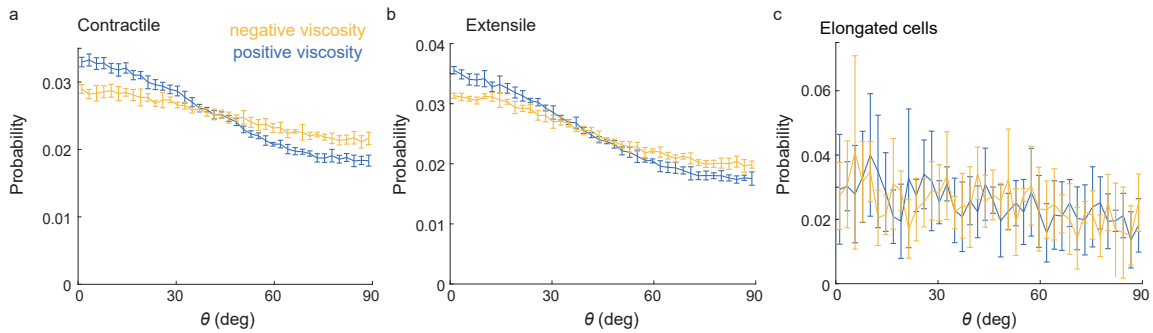


**Figure 9:** (a, b) Alignment of stress and flow for contractile and extensile cells. Contractile and extensile regions in the cell layer were determined as described previously.<sup>26</sup> The histograms show the distribution of  $\theta$ , the angle between orientations of  $\sigma_2$  and  $\dot{\epsilon}_1$ , in contractile (a) and extensile (b) regions for regions of positive and negative viscosity. (c) Distribution of angle  $\theta$  for elongated cells. Histograms show the distributions of  $\theta$  from 6 cell islands over 15 hr of imaging. Error bars represent the standard deviation of the probability values for each bin, calculated across all cell islands.

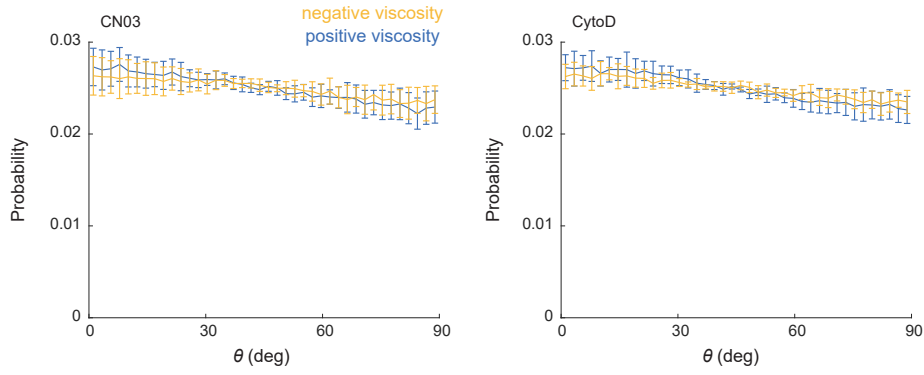


**Figure 10:** Alignment of stress and flow in response to perturbations of force production. Distributions of  $\theta$ , the angle between orientations of  $\sigma_2$  and  $\dot{\epsilon}_1$ , in cells treated with CN03 (left) and cytoD (right) for regions of positive and negative viscosity. Histograms show the distributions of  $\theta$  from 6 cell islands over 15 hr of imaging. Error bars represent the standard deviation of the probability values for each bin, calculated across all cell islands.

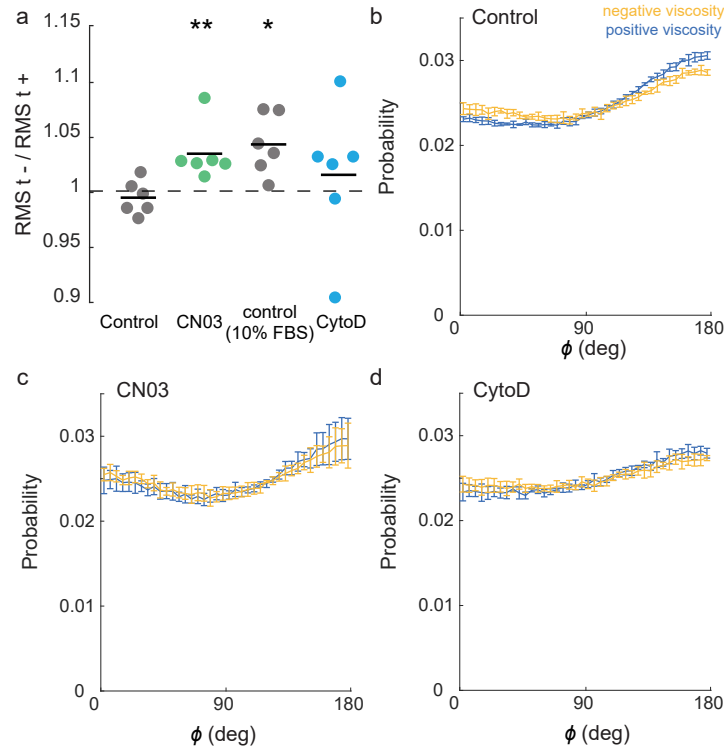


**Figure 11:** Traction in regions of positive and negative viscosity. (a) Ratio of RMS traction in regions of negative viscosity to regions of positive viscosity for the control, CN03, 10% FBS control, and cytoD treated groups (Control  $p = 0.058$ , CN03  $p = 0.004$ , Control 10% FBS  $p = 0.012$ , CytoD  $p = 0.234$ , one-sample t-test in comparison to 1). A dot indicates the mean of a cell island over time and black bars indicate means. (b–d) The angle between substrate-to-cell traction and velocity,  $\phi$ , in regions of positive and negative viscosity for the control case and treatments with CN03 and cytoD. Histograms show the distributions of  $\phi$  from 6 cell islands over 15 hr of imaging. Error bars represent the standard deviation of the probability values for each bin, calculated across all cell islands.

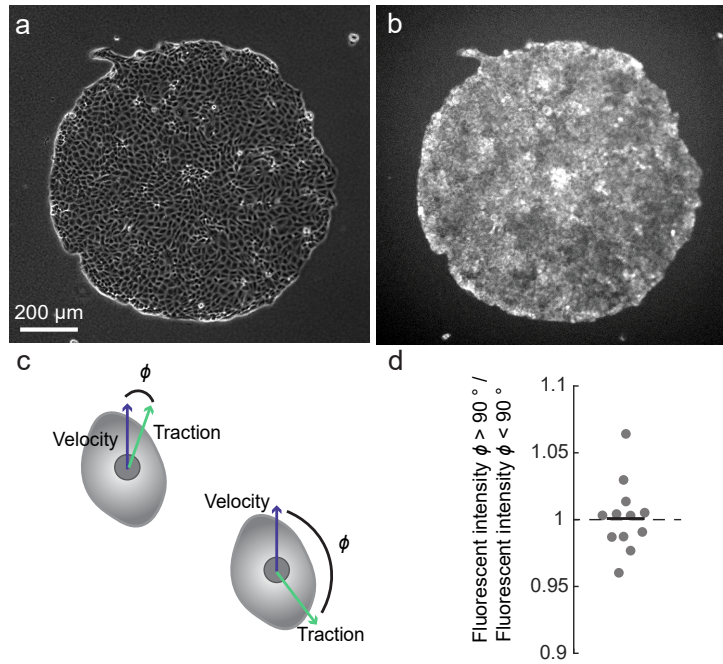


**Figure 12:** Mitochondrial membrane potential in locations where substrate-to-cell tractions propel and resist the flow. (a) Phase contrast image of a cell island. (b) Image of TMRE intensity, showing mitochondrial membrane potential. (c) Cartoon depicting cells with traction and velocity aligned (left,  $\phi < 90^\circ$ ), and traction and velocity are misaligned (right,  $\phi > 90^\circ$ ). (d) Ratio of fluorescent intensity in regions where velocity and traction are misaligned ( $\phi > 90^\circ$ ) to regions where velocity and traction are aligned ( $\phi < 90^\circ$ ) ( $p = 0.787$ , one-sample t-test in comparison to 1).



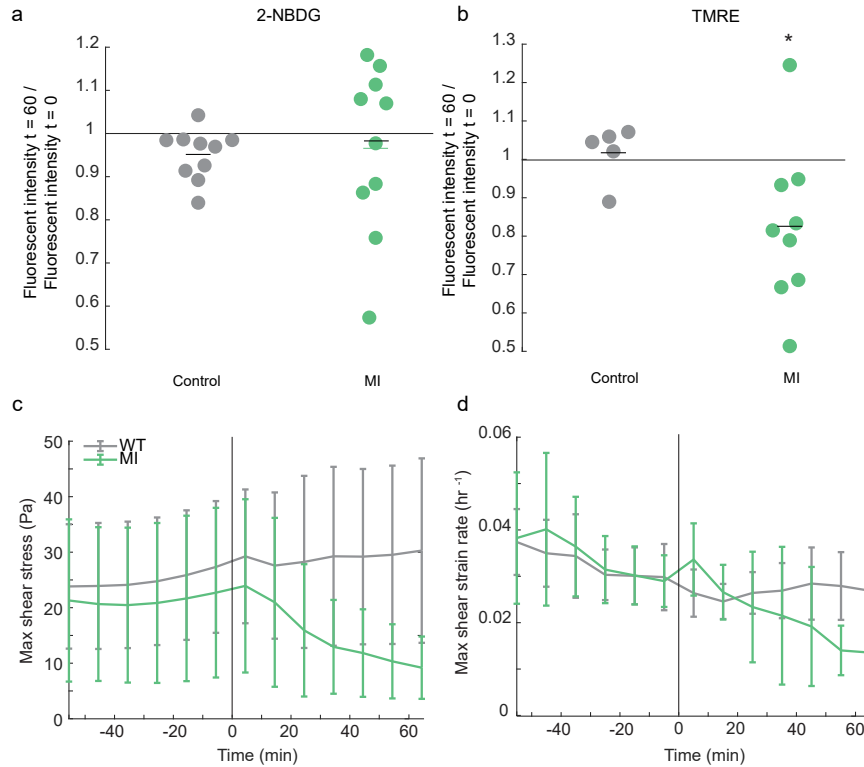


**Figure 13:** Effects of metabolic inhibition. (a, b) Ratio of fluorescent intensity 60 min after ( $t = 60$  min) to immediately before ( $t = 0$ ) spike with vehicle control and metabolic inhibitors, for 2-NBDG (glucose uptake) and TMRE (mitochondrial membrane potential). Metabolic inhibition caused a decrease in TMRE fluorescent intensity compared to control, indicating a decrease in mitochondrial function (TMRE, Control  $p = 0.617$ , MI  $p = 0.020$  compared to 1, one-sample t-test). (c, d) Shear stress and shear strain rate over time for control (gray) and metabolic inhibition (green) cases. The metabolic inhibitors (or vehicle control) were added at time 0. Lines represent means and error bars represent standard deviations over different cell islands.

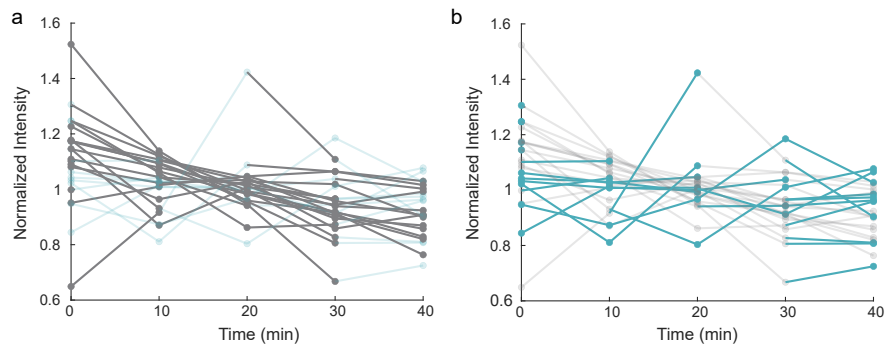


**Figure 14:** Fluorescent intensity of TMRE over time. Each line indicates a randomly chosen  $62 \times 62 \mu\text{m}^2$  ROI. Gray and blue line segments indicate times over which the ROI has positive and negative viscosity, respectively. Fluorescent intensity in each ROI was normalized by the mean over all time points in that ROI. These data are the same as shown as in Fig. 4h, and, for visual clarity, line transparency has been adjusted: (a) negative viscosity lines are more transparent, and (b) positive viscosity lines are more transparent. In panel a, gray lines (corresponding to positive viscosity) typically have negative slope, whereas in panel b, blue lines (corresponding to negative viscosity) typically have a slope of approximately 0.

## References

- [1] Poujade, M., Grasland-Mongrain, E., Hertzog, A., Jouanneau, J., Chavrier, P., Ladoux, B., Buguin, A., and Silberzan, P. Collective migration of an epithelial monolayer in response to a model wound. *P Natl Acad Sci USA*, 104(41):15988–15993, 2007.
- [2] Vedula, S. R. K., Leong, M. C., Lai, T. L., Hersen, P., Kabla, A. J., Lim, C. T., and Ladoux, B. Emerging modes of collective cell migration induced by geometrical constraints. *P Natl Acad Sci USA*, 109(32):12974–12979, 2012.
- [3] Alert, R., Casademunt, J., and Joanny, J.-F. Active turbulence. *Annu Rev Condens Matter Phys*, 13(10.1146):143–170, 2022.
- [4] Trepats, X., Wasserman, M. R., Angelini, T. E., Millet, E., Weitz, D. A., Butler, J. P., and Fredberg, J. J. Physical forces during collective cell migration. *Nat Phys*, 5(6):426–430, 2009.
- [5] Tambe, D. T., Hardin, C. C., Angelini, T. E., Rajendran, K., Park, C. Y., Serra-Picamal, X., Zhou, E. H., Zaman, M. H., Butler, J. P., Weitz, D. A., Fredberg, J. J., and Trepats, X. Collective cell guidance by cooperative intercellular forces. *Nat Mater*, 10(6):469–475, 2011.
- [6] Kim, J. H., Serra-Picamal, X., Tambe, D. T., Zhou, E. H., Park, C. Y., Sadati, M., Park, J.-A., Krishnan, R., Gweon, B., Millet, E., Butler, J. P., Trepats, X., and Fredberg, J. J. Propulsion and navigation within the advancing monolayer sheet. *Nat Mater*, 12(9):856–863, 2013.
- [7] Marchetti, M. C., Joanny, J.-F., Ramaswamy, S., Liverpool, T. B., Prost, J., Rao, M., and Simha, R. A. Hydrodynamics of soft active matter. *Rev Mod Phys*, 85(3):1143, 2013.
- [8] Alert, R. and Trepats, X. Physical models of collective cell migration. *Annu Rev Condens Matter Phys*, 11(1):77–101, 2020.
- [9] Duclos, G., Erenkämper, C., Joanny, J.-F., and Silberzan, P. Topological defects in confined populations of spindle-shaped cells. *Nat Phys*, 13(1):58–62, 2017.
- [10] Pérez-González, C., Alert, R., Blanch-Mercader, C., Gómez-González, M., Kolodziej, T., Bazellieres, E., Casademunt, J., and Trepats, X. Active wetting of epithelial tissues. *Nat Phys*, 15(1):79–88, 2019.
- [11] Marmottant, P., Mgharbel, A., Käfer, J., Audren, B., Rieu, J.-P., Vial, J.-C., van der Sanden, B., Marée, A. F. M., Graner, F., and Delanoë-Ayari, H. The role of fluctuations and stress on the effective viscosity of cell aggregates. *P Natl Acad Sci USA*, 106(41):17271–17275, 2009.
- [12] Guevorkian, K., Colbert, M.-J., Durth, M., Dufour, S., and Brochard-Wyart, F. Aspiration of biological viscoelastic drops. *Phys Rev Lett*, 104(21):218101, 2010.
- [13] Blanch-Mercader, C., Vincent, R., Bazellieres, E., Serra-Picamal, X., Trepats, X., and Casademunt, J. Effective viscosity and dynamics of spreading epithelia: a solvable model. *Soft Matter*, 13(6):1235–1243, 2017.
- [14] Notbohm, J., Banerjee, S., Utuje, K. J., Gweon, B., Jang, H., Park, Y., Shin, J., Butler, J. P., Fredberg, J. J., and Marchetti, M. C. Cellular contraction and polarization drive collective cellular motion. *Biophys J*, 110(12):2729–2738, 2016.
- [15] Saraswathibhatla, A. and Notbohm, J. Traction and stress fibers control cell shape and rearrangements in collective cell migration. *Phys Rev X*, 10(1):011016, 2020.

- [16] Tambe, D. T., Croutelle, U., Trepate, X., Park, C. Y., Kim, J. H., Millet, E., Butler, J. P., and Fredberg, J. J. Monolayer stress microscopy: limitations, artifacts, and accuracy of recovered intercellular stresses. *Plos One*, 8(2):e55172, 2013.
- [17] Saraswathibhatla, A., Galles, E. E., and Notbohm, J. Spatiotemporal force and motion in collective cell migration. *Sci Data*, 7(1):197, 2020.
- [18] Hatwalne, Y., Ramaswamy, S., Rao, M., and Simha, R. A. Rheology of active-particle suspensions. *Phys Rev Lett*, 92(11):118101, 2004.
- [19] Cates, M., Fielding, S., Marenduzzo, D., Orlandini, E., and Yeomans, J. Shearing active gels close to the isotropic-nematic transition. *Phys Rev Lett*, 101(6):068102, 2008.
- [20] Sokolov, A. and Aranson, I. S. Reduction of viscosity in suspension of swimming bacteria. *Phys Rev Lett*, 103(14):148101, 2009.
- [21] Gachelin, J., Mino, G., Berthet, H., Lindner, A., Rousselet, A., and Clément, É. Non-newtonian viscosity of escherichia coli suspensions. *Phys Rev Lett*, 110(26):268103, 2013.
- [22] López, H. M., Gachelin, J., Douarche, C., Auradou, H., and Clément, E. Turning bacteria suspensions into superfluids. *Phys Rev Lett*, 115(2):028301, 2015.
- [23] Orihara, H., Harada, Y., Kobayashi, F., Sasaki, Y., Fujii, S., Satou, Y., Goto, Y., and Nagaya, T. Negative viscosity of a liquid crystal in the presence of turbulence. *Phys Rev E*, 99(1):012701, 2019.
- [24] Chui, J. Y., Douarche, C., Auradou, H., and Juanes, R. Rheology of bacterial superfluids in viscous environments. *Soft Matter*, 17(29):7004–7013, 2021.
- [25] Saintillan, D. Rheology of active fluids. *Annu Rev Fluid Mech*, 50(1):563–592, 2018.
- [26] Nejad, M. R., Ruske, L. J., McCord, M., Zhang, J., Zhang, G., Notbohm, J., and Yeomans, J. M. Stress-shape misalignment in confluent cell layers. *Nat Commun*, 15(1):3628, 2024.
- [27] Lee, P. and Wolgemuth, C. Advent of complex flows in epithelial tissues. *Phys Rev E*, 83(6):061920, 2011.
- [28] Cochet-Escartin, O., Ranft, J., Silberzan, P., and Marcq, P. Border forces and friction control epithelial closure dynamics. *Biophys J*, 106(1):65–73, 2014.
- [29] Pérez-González, C., Alert, R., Blanch-Mercader, C., Gómez-González, M., Kolodziej, T., Bazellieres, E., Casademunt, J., and Trepate, X. Active wetting of epithelial tissues. *Nat Phys*, 15(1):79–88, 2019.
- [30] Vazquez, K., Saraswathibhatla, A., and Notbohm, J. Effect of substrate stiffness on friction in collective cell migration. *Sci Rep*, 12(1):2436, 2022.
- [31] Lin, S.-Z., Zhang, W.-Y., Bi, D., Li, B., and Feng, X.-Q. Energetics of mesoscale cell turbulence in two-dimensional monolayers. *Commun Phys*, 4(1):21, 2021.
- [32] Scaduto, R. C. and Grotyohann, L. W. Measurement of Mitochondrial Membrane Potential Using Fluorescent Rhodamine Derivatives. *Biophys J*, 76(1):469–477, 1999.
- [33] Zou, C., Wang, Y., and Shen, Z. 2-NBDG as a fluorescent indicator for direct glucose uptake measurement. *J Biochem Bioph Meth*, 64(3):207–215, 2005.

- [34] DeCamp, S. J., Tsuda, V. M. K., Ferruzzi, J., Koehler, S. A., Giblin, J. T., Roblyer, D., Zaman, M. H., Weiss, S. T., Kılıç, A., De Marzio, M., Park, C. Y., Ogassavara, N. C., Mitchel, J. A., Butler, J. P., and Fredberg, J. J. S epithelial layer unjamming shifts energy metabolism toward glycolysis. *Sci Rep*, 10(1):18302, 2020.
- [35] Baron, S., Caplanusi, A., van de Ven, M., Radu, M., Despa, S., Lambrichts, I., Ameloot, M., Steels, P., and Smets, I. Role of mitochondrial  $\text{na}^+$  concentration, measured by CoroNa red, in the protection of metabolically inhibited MDCK cells. *J Am Soc Nephrol*, 16(12):3490, 2005.
- [36] Wensink, H. H., Dunkel, J., Heidenreich, S., Drescher, K., Goldstein, R. E., Löwen, H., and Yeomans, J. M. Meso-scale turbulence in living fluids. *P Natl Acad Sci USA*, 109(36):14308–14313, 2012.
- [37] Rossen, N. S., Tarp, J. M., Mathiesen, J., Jensen, M. H., and Oddershede, L. B. Long-range ordered vorticity patterns in living tissue induced by cell division. *Nat Commun*, 5(1):5720, 2014.
- [38] Smart, A. G., Amaral, L. A., and Ottino, J. M. Cascading failure and robustness in metabolic networks. *P Natl Acad Sci USA*, 105(36):13223–13228, 2008.
- [39] Stelling, J., Sauer, U., Szallasi, Z., Doyle, F. J., and Doyle, J. Robustness of cellular functions. *Cell*, 118(6):675–685, 2004.
- [40] Whitacre, J. M. Biological robustness: paradigms, mechanisms, and systems principles. *Front Genet*, 3:67, 2012.
- [41] DeBerardinis, R. J. and Chandel, N. S. Fundamentals of cancer metabolism. *Sci Adv*, 2(5):e1600200, 2016.
- [42] Bergers, G. and Fendt, S.-M. The metabolism of cancer cells during metastasis. *Nat Rev Cancer*, 21(3):162–180, 2021.
- [43] Saraswathibhatla, A., Henkes, S., Galles, E. E., Sknepnek, R., and Notbohm, J. Coordinated tractions increase the size of a collectively moving pack in a cell monolayer. *Extreme Mech Lett*, 48:101438, 2021.
- [44] Bar-Kochba, E., Toyjanova, J., Andrews, E., Kim, K.-S., and Franck, C. A fast iterative digital volume correlation algorithm for large deformations. *Exp Mech*, 55(1):261–274, 2015.
- [45] Butler, J. P., Tolic-Norrelykke, I. M., Fabry, B., and Fredberg, J. J. Traction fields, moments, and strain energy that cells exert on their surroundings. *Am J Physiol Cell Ph*, 282(3):C595–C605, 2002.
- [46] del Alamo, J. C., Meili, R., Alonso-Latorre, B., Rodriguez-Rodriguez, J., Aliseda, A., Firtel, R. A., and Lasheras, J. C. Spatio-temporal analysis of eukaryotic cell motility by improved force cytometry. *P Natl Acad Sci USA*, 104(33):13343–13348, 2007.
- [47] J.Vromans, A. and Giomi, L. Orientational properties of nematic disclinations. *Soft Matter*, 12(30):6490–6495, 2016.
- [48] Saraswathibhatla, A., Zhang, J., and Notbohm, J. Coordination of contractile tension and cell area changes in an epithelial cell monolayer. *Phys Rev E*, 105(2):024404, 2022.
- [49] Smets, I., Caplanusi, A., Despa, S., Molnar, Z., Radu, M., vandeVen, M., Ameloot, M., and Steels, P.  $\text{Ca}^{2+}$  uptake in mitochondria occurs via the reverse action of the  $\text{Na}^{2+}/\text{Ca}^{2+}$  exchanger in metabolically inhibited MDCK cells. *Am J Physiol Renal Physiol*, 286(4):F784–F794, 2003.

- [50] Bi, D., Yang, X., Marchetti, M. C., and Manning, M. L. Motility-driven glass and jamming transitions in biological tissues. *Phys Rev X*, 6(2):021011, 2016.